Nuclear Science and Techniques (2024) 35:203
https://doi.org/10.1007/s41365-024-01580-5

Improved isochronous mass spectrometry with tune measurement

Han-Yu Deng[1,2] · Yuan-Ming Xing[1,2] · Xu Zhou[1,2] · Yu-Hu Zhang[1,2] · Xin-Liang Yan[1,2] · Jin-Yang Shi[1,2] · Ting Liao[1,2] · Meng Wang[1,2]

Received: 24 June 2024 / Revised: 20 August 2024 / Accepted: 1 September 2024 / Published online: 16 October 2024

Abstract
In conventional isochronous mass spectrometry (IMS) performed on a storage ring, the precision of mass measurements for short-lived nuclei depends on the accurate determination of the revolution times (T) of stored ions. However, the resolution of T inevitably deteriorates due to the magnetic rigidity spread of the ions, limiting the mass-resolving power. In this study, we used the betatron tunes Q (the number of betatron oscillations per revolution) of the ions and established a correlation between T and Q. From this correlation, T was transformed to correspond to a fixed Q with higher resolution. Using these transformed T values, the masses of ^{63}Ge, ^{65}As, ^{67}Se, and ^{71}Kr agreed well with the mass values measured using the newly developed IMS ($B\rho$-IMS). We also studied the systematics of Coulomb displacement energies (CDEs) and found that anomalous staggering in CDEs was eliminated using new mass values. This method of T transformation is highly effective for conventional IMS equipped with a single time-of-flight detector.

Keywords Isochronous Mass Spectrometry · Storage ring · Tune · Natural chromaticity · Nuclear mass measurement

1 Introduction

Mass is a fundamental property of atomic nuclei and plays a crucial role in studies of nuclear structure and nuclear astrophysics [1, 2]. Significant efforts have been devoted to developing mass-measurement technologies, particularly for short-lived nuclides [3, 4]. Isochronous mass spectrometry (IMS) [5, 6] on heavy-ion storage rings has proven to be a powerful tool, providing numerous new mass values for short-lived nuclides [7–12].

In conventional IMS equipped with a single time-of-flight (TOF) detector, nuclear masses are determined by measuring the revolution times (T) of ions stored in the ring. Given that a storage ring operates within a certain acceptance of magnetic rigidity $B\rho$ (or momentum p), stored ions of the same species exhibit a velocity spread. Although ions with higher velocities are expected to circulate in the ring along larger orbital paths and vice versa, the revolution time of ions in different orbits will still differ if the velocity variation is not perfectly compensated by variations in orbital length. This velocity spread results in a broad distribution of T. The dependence of T on velocity can be effectively removed for ions that satisfy isochronous conditions [5]. However, for most ions, the velocity dependence of T leads to significant

This work is supported in part by the National Key R&D Program of China (No. 2023YFA1606401), CAS Project for Young Scientists in Basic Research (No. YSBR-002), Strategic Priority Research Program of the Chinese Academy of Sciences (No. XDB34000000), and the NSFC (Nos. 12305126, 12135017, 12121005). Y.M.X. acknowledges the support from the Youth Innovation Promotion Association of the Chinese Academy of Sciences (No. 2021419). X.L.Y. acknowledges the support from the Yong Scholar of Regional Development, CAS (No.[2023]15).

✉ Yuan-Ming Xing
xym@impcas.ac.cn

✉ Xu Zhou
zhouxu@impcas.ac.cn

✉ Meng Wang
wangm@impcas.ac.cn

[1] CAS Key Laboratory of High Precision Nuclear Spectroscopy, Institute of Modern Physics, Chinese Academy of Sciences, Lanzhou 730000, China

[2] School of Nuclear Science and Technology, University of Chinese Academy of Sciences, Beijing 100049, China

deterioration in mass precision and may introduce systematic errors [13] in the measured masses.

To reduce the effect of velocity spread on the T distribution and enhance the performance of IMS, several methods have been proposed. One such method, known as $B\rho$-tagging IMS [14], employs a mechanical slit at the dispersive focal plane of the beam line or in the ring to restrict the $B\rho$ acceptance, thereby narrowing the T distribution [14, 15]. However, this approach reduces transmission efficiency and is unfavorable for mass measurements of exotic nuclei with extremely low production yields. Another method, referred to as $B\rho$-defined IMS or $B\rho$-IMS [13, 16], employs two TOF detectors to measure the velocity of ions directly and determine $B\rho$ values [17]. With the measured $B\rho$ and velocity, the mass-to-charge ratio m/q of the ions is calculated, resulting in improved mass-resolving power [13, 16]. However, compared to conventional IMS utilizing only one TOF detector, $B\rho$-IMS introduces double the energy loss for ions during each revolution. Since energy loss increases with proton number, heavier ions experience more pronounced losses. Repeated traversal through the carbon foils of the two detectors can cause the ion momentum to exceed the storage ring's acceptance range, leading to ion loss and a significant reduction in storage time, complicating the precise determination of ion velocity and $B\rho$. Additionally, the installation of two TOF detectors in a straight section of the ring presents practical challenges, such as the precise determination of the distance between detectors and managing time delay differences [18]. Furthermore, a previous study revealed that using a single oscilloscope to record flight time signals is necessary to avoid jitter at the start times of two oscilloscopes [19]. However, using only one oscilloscope introduces other issues, such as signal attenuation due to longer cables and excessive writing times caused by the large volume of data being recorded.

In this paper, we introduce a new method called Tune-IMS to improve conventional IMS. The motion of a charged particle with nonzero emittance in a storage ring exhibits betatron oscillations around a closed orbit [20, 21]. The number of oscillations per revolution, known as the tune (Q) value, is directly related to the ions' $B\rho$ and their revolution time T [21]. A previous study [22] proposed a method for measuring Q using a single TOF detector. By using the correlation between T and Q for each ion species, the measured T can be transformed into a new revolution time, T_Q, corresponding to a reference closed orbit with a fixed Q. As a result, for ions that do not satisfy the isochronous condition, the new T_Q distribution is narrower, leading to improved mass-resolving power.

In this study, we briefly present the principle of this method and apply it to an IMS experiment [23, 24] conducted at the experimental cooling storage ring (CSRe) of the Heavy Ion Research Facility in Lanzhou (HIRFL-CSR). The re-determined mass values of ^{63}Ge, ^{65}As, ^{67}Se and ^{71}Kr with higher precision were compared with those from a recent $B\rho$-IMS experiment [25, 26]. The Coulomb displacement energies (CDEs) extracted from these new mass values were also compared with theoretical estimates.

2 Principle of Tune-IMS

Under ideal conditions in a stable magnetic field, the magnetic rigidity $B\rho$, revolution time T, and tune Q are uniquely determined for a specific ion circling a closed orbit. If the closed orbit of the same ion is slightly altered, the corresponding variation in T with $B\rho$ (denoted as ΔT and $\Delta B\rho$, respectively) is described by [27]:

$$\frac{\Delta T}{T} = \left(\frac{1}{\gamma_t^2} - \frac{1}{\gamma^2}\right)\frac{\Delta B\rho}{B\rho} = -\eta\frac{\Delta B\rho}{B\rho}, \tag{1}$$

where γ_t represents the transition point of the ring, γ is the Lorentz factor, and $\eta \equiv 1/\gamma^2 - 1/\gamma_t^2$ is the phase-slip factor. As shown in Eq. (1), for ions satisfying the isochronicity condition where $\gamma \approx \gamma_t$ (or $\eta \approx 0$), ΔT is independent of $\Delta B\rho$, achieving a relatively high resolution of T. However, for most ions where $\eta \neq 0$, variations in $B\rho$ results in corresponding changes in T. This leads to a deterioration in T which may introduce systematic deviations in the obtained mass values [13].

In contrast, the tune number Q represents the betatron oscillations around the closed orbit. In a linear storage ring equipped solely with dipoles and quadrupoles, the ratio of variations in Q (denoted as ΔQ) to variations in $\Delta B\rho/B\rho$ (or equivalently, $\Delta p/p$), is defined as the natural chromaticity ξ [28]:

$$\xi \equiv \frac{\Delta Q}{\Delta B\rho/B\rho}. \tag{2}$$

According to Eqs. (1) and (2), the correlation between T and Q can be expressed as follows:

$$\Delta T = -\eta T\frac{\Delta Q}{\xi}. \tag{3}$$

Thus, each (T, Q) set corresponding to the closed orbit can be approximated as (T_Q, Q_0), where T_Q corresponds to a reference closed orbit with a fixed tune value, Q_0:

$$T_Q = T - \Delta T = T\left(1 + \eta\frac{\Delta Q}{\xi}\right). \tag{4}$$

Thus, if ΔQ, ξ and η are properly determined, the effect of $B\rho$ spread on T can be corrected.

3 Experimental results

3.1 Measurement of *T*

The new tune-IMS method was applied to an early IMS experiment conducted at the HIRFL-CSR [23, 24]. In the experiment, a $^{78}Kr^{28+}$ beam was accelerated to 483 MeV/u and bombarded with a 15-mm thick beryllium target. The fragments, predominantly bare ions, were selected using the second Radioactive Ion Beam Line at Lanzhou (RIBLL2) and injected into the CSRe (see Fig. 1). The magnetic rigidity $B\rho$ of the RIBLL2-CSRe system was set to 5.9464 Tm, and the transition point γ_t of CSRe was set to 1.406.

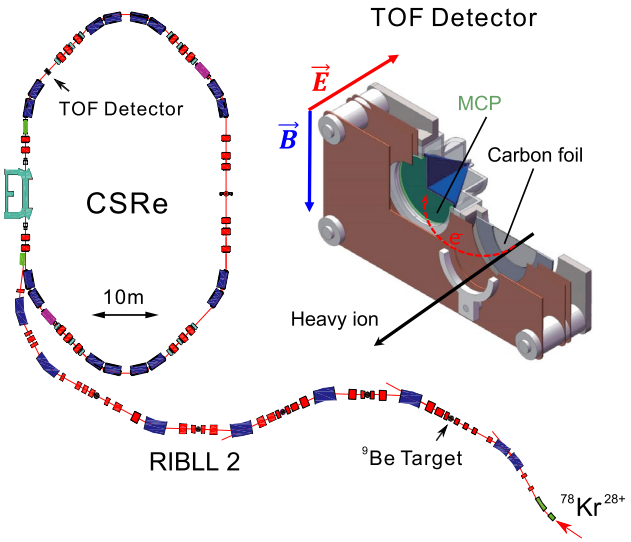

Fig. 1 (Color online) Layout of RIBLL2 and CSRe, along with a schematic diagram of the TOF detector [11]

A TOF detector equipped with a 19-μg/cm^2 thin carbon foil was installed in the CSRe [29]. Each ion passes through the detector, releasing secondary electrons from the foil, which are then transmitted isochronously through perpendicularly arranged electric and magnetic fields to a microchannel plate (MCP) counter. The electrical signal from the MCP anode was directed to a fast digital oscilloscope for full-waveform sampling without amplification. The detection efficiency of the signal at each revolution turn mainly depends on the atomic number of the ions. After each injection, a measurement time of 200 μs was set, corresponding to approximately 300 turns for the ions stored in the CSRe. For each ion, a time sequence $t(N)$ as a function of turn number N was obtained.

To account for energy loss, a third-order polynomial was fitted to the $t(N)$ sequence. In this case, T is the first derivative of $t(N)$ at a specific N, such as the middle of the ion's full storage period.

In reality, the magnetic field instability can induce drifts in T. This study used the method reported in Refs. [30] to correct T drifts caused by unstable magnetic fields. Compared to the previous approach [24], this method can handle injections with only a few stored ions. A portion of the obtained T-spectrum is shown in Fig. 2.

3.2 Determination of *Q* and *ξ*

The method for measuring Q and ξ using a single TOF detector is described in detail in Refs.[22]. The remainder of this paper is organized as follows:

Due to betatron oscillations, the time sequence $t(N)$ recorded by the TOF detector includes an oscillation term [17]. Using a $^{51}Fe^{26+}$ ion measured in this experiment as an example, Fig. 3 shows the results obtained by applying a Digital Fourier Transform (DFT) [22, 31] to the residuals

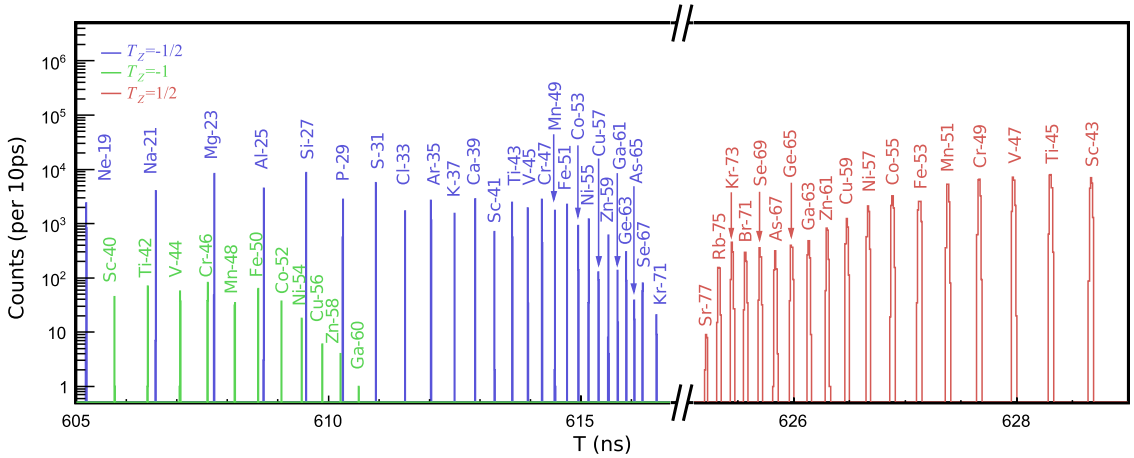

Fig. 2 (Color online) Revolution time spectrum within the range of 605 ns $\leq T \leq$ 629 ns. Different colours indicate nuclei with different isospin projections $T_z = (N - Z)/2$. The $N = Z$ nuclei with $T \sim 620$ ns are not shown due to difficulties in particle identification

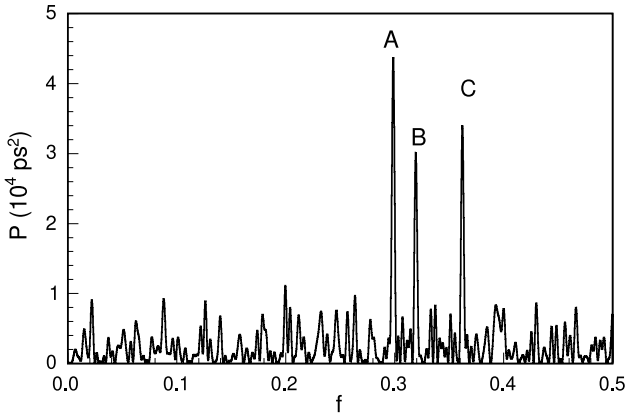

Fig. 3 Result of the Fourier transform applied to the fitting residuals of the time sequences for a $^{51}Fe^{26+}$ ion is shown. Three significant peaks, labeled A, B, and C, were identified within the frequency range $0 \leq f \leq 0.5$. Since the time sequence is sampled once per revolution, the DFT analysis can only detect periodic components within the frequency range of 0–0.5, according to the Nyquist–Shannon sampling theorem [32]

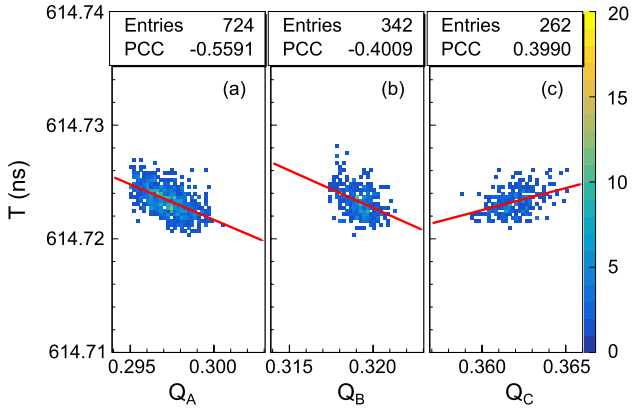

Fig. 4 (Color online) Scatter plots of T against Q_i (where i spans A, B, C) for all $^{51}Fe^{26+}$ ions are shown. Each subplot includes the data entries and the PCC [33]. The red lines represent the results of linear fitting

of $t(N)$ fitted with a third-order polynomial. Three significant peaks, labeled A, B, and C, were identified, indicating three periodic components within the time sequence. This analysis was applied to all recorded time sequences, consistently revealing a three-peak pattern.

A detailed study of the origin of these peaks can be found in Ref. [22]. To accurately model the three periodic components, a comprehensive fitting function [17] was employed to refit the passing time sequences as follows:

$$\begin{aligned} t_{\mathrm{fit}}(N) = {} & a_0 + a_1 \cdot N + a_2 \cdot N^2 + a_3 \cdot N^3 \\ & + A_{\mathrm{A}} \cdot \sin[2\pi \cdot (Q_{\mathrm{A0}} \cdot N + Q_{\mathrm{A1}} \cdot N^2) + \phi_{\mathrm{A}}] \\ & + A_{\mathrm{B}} \cdot \sin[2\pi \cdot (Q_{\mathrm{B0}} \cdot N + Q_{\mathrm{B1}} \cdot N^2) + \phi_{\mathrm{B}}] \\ & + A_{\mathrm{C}} \cdot \sin[2\pi \cdot (Q_{\mathrm{C0}} \cdot N + Q_{\mathrm{C1}} \cdot N^2) + \phi_{\mathrm{C}}]. \end{aligned} \tag{5}$$

Here, sine-like terms account for the oscillations, where A_i and ϕ_i (i corresponds to A, B, C) represent the amplitudes and initial phases of the periodic components, respectively. The first derivative of each phase term,

$$Q_i = Q_{i0} + 2Q_{i1} \cdot N, \tag{6}$$

corresponds to the fractional tune at each N [17], where Q_{i0} is the fractional tune value and Q_{i1} is a factor accounting for energy loss as the ion passes through the carbon foil of the TOF detector [17]. Similar to the determination of T, the middle turn number was used to determine Q_i.

The accuracy of the measured Q_i value depends on the amplitude A_i of the oscillation component, which is proportional to the square root of the emittance [22]. For ions with low emittance, the amplitude of the betatron oscillation is small, resulting in low peaks in the $P(f)$-spectrum. Moreover, for lighter ions with lower charge numbers, the detection efficiency of the time signals was significantly reduced, increasing the background noise in the $P(f)$ spectrum. We defined the signal-to-noise ratio as the ratio of the peak amplitude to the mean amplitude of the background noise. Obviously, a low signal-to-noise ratio can lead to inaccurate determination of the Q value. Therefore, only the (T, Q_i) datasets with a signal-to-noise ratio exceeding 7 were used for further analyses.

Using all $^{51}Fe^{26+}$ ions as an example, Fig. 4 presents scatter plots of the selected Q_i against T, revealing a clear correlation. As shown in the figure, Q_{A} exhibits the highest counts and Pearson correlation coefficients (PCC) [33]. Consequently, Q_{A} was selected for subsequent analyses.

According to Eq. (3), we obtain

$$-\eta T = \xi \frac{\Delta T}{\Delta Q}. \tag{7}$$

As ξ is a machine parameter of the storage ring and is independent of the ion species, ξ is the slope if $-\eta T$ is plotted as a linear function of $\Delta T/\Delta Q$ for different ion species: 1) $\Delta T/\Delta Q$, the rate of change of T with respect to Q, can be estimated as the slope of the linear function fitted to T vs Q_{A} (see the red fitting line in Fig. 4 (a) for $^{51}Fe^{26+}$, for example). 2) η is calculated as $1/\gamma^2 - 1/\gamma_{\mathrm{t}}^2$, with $\gamma_{\mathrm{t}} = 1.406$. To obtain γ, the velocity was estimated as $\overline{C}/\overline{T}$, where $\overline{C}$ is the average orbit length determined using the method introduced in Ref. [30] and $\overline{T}$ is the average T value for each ion species. Figure 5 shows a plot of $-\eta T$ as a function of $\Delta T/\Delta Q$. The average chromaticity ξ, extracted from the slope of the linear fit shown in Fig. 5, is 4.87 (3).

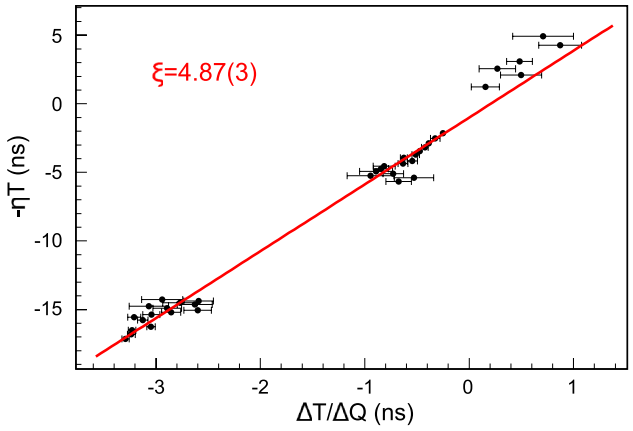

Fig. 5 Plot of $-\eta T$ against $\Delta T/\Delta Q$ for all ion species is shown. Each point marker represents one ion species. The linear fitting function is presented as a red solid line. The slope of this line, which represents the average chromaticity ξ according to Eq. (3), is also noted

3.3 The *T* transformation and the mass determination

Using Eq. (4), the measured (T, Q_{A}) values for each ion were transformed into (T_Q, Q_{A0}) at a fixed $Q_{\mathrm{A0}} = 0.298$, which is the mean of all Q_{A} values.

Figure 6 illustrates the standard deviation (σ) of T and T_Q for each ion species, corresponding to the revolution times before and after the transformation, respectively. As shown in Fig. 6, the farther an ion species is from the one with the minimum $\sigma(T)$, the larger the ratio of $\sigma(T)/\sigma(T_Q)$. For ion species with $T \approx 629$ ns, $\sigma(T)$ decreases by up to a factor of 2.5 to $\sigma(T_Q)$. Consequently, the mass-resolving power of these ion species was improved by the same factor. However, for ion species with η values close to zero, the decrease from $\sigma(T)$ to $\sigma(T_Q)$ is almost negligible (see Eq. 3).

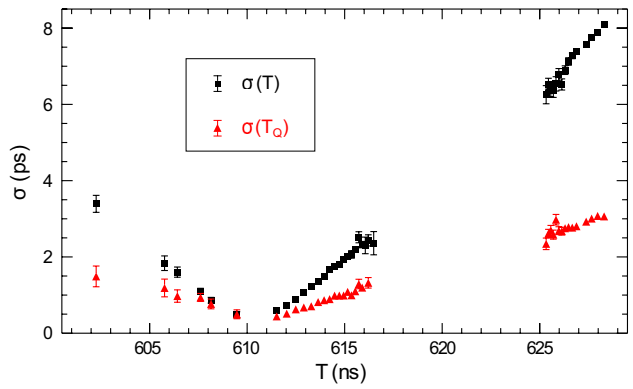

Fig. 6 Standard deviation of the revolution time before and after transformation using Eq. (4) is denoted as $\sigma(T)$ (black filled squares) and $\sigma(T_Q)$ (red filled triangles), respectively

Using both T and T_Q, the mass of each nuclide was determined following the procedure outlined in Ref. [35]. Figure 7 shows the differences between the redetermined MEs and the literature values [34] for all reference nuclides. To assess the agreement, the χ_n value is defined as

$$\chi_n = \sqrt{\frac{1}{N_{\mathrm{c}}} \sum_{i=1}^{N_{\mathrm{c}}} \frac{\left(ME_i - ME_{\mathrm{AME20},i}\right)^2}{\sigma_i^2 + \sigma_{\mathrm{AME20},i}^2}}. \tag{8}$$

Here, $N_{\mathrm{c}} = 27$ represents the number of calibrants, and σ_i and $\sigma_{\mathrm{AME20},i}$ denote the 1σ uncertainties of ME_i and $ME_{\mathrm{AME20},i}$, respectively.

For the re-determined MEs using T, the calculated $\chi_n = 1.35$ exceeds the 1σ confidence level of $\chi_n = 1 \pm 1/\sqrt{2N_{\mathrm{c}}} = 1 \pm 0.14$, indicating that an additional systematic error of 13.1 keV should be considered. In contrast, when using T_Q, χ_n value is reduced to 0.97(14), suggesting that no additional systematic errors are necessary. Table 1 summarizes the final ME values and counts determined for ^{63}Ge, ^{65}As, ^{67}Se, and ^{71}Kr using T and T_Q. The table also includes results from a previous IMS study (CSRe2011) [23] and the most recent $B\rho$-IMS experiment (CSRe2023) [25, 26].

For comparison, *ME* values are shown in Fig. 8, with recent CSRe2023 results serving as a benchmark. Compared to the results from CSRe2011 and those using T, the results using T_Q not only align more closely with CSRe2023 but also exhibit higher precision. The improvements in accuracy and precision are mainly due to the significantly reduced spread of T_Q, as shown in Fig. 6, despite the lower statistics reported in Table 1. Notably, the mass precision using T_Q is comparable to that achieved with the advanced $B\rho$-IMS method used in CSRe2023.

Notably, for ^{63}Ge, the ME value obtained using T exhibits a significant deviation compared to CSRe2023. Although the discrepancy is reduced with T_Q, it remains

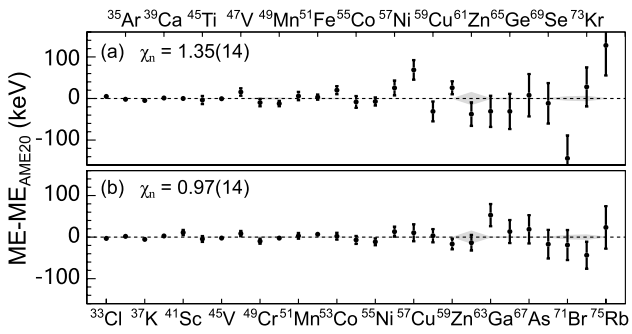

Fig. 7 Comparison of the re-determined mass excess (ME) values with the literature values (ME_{AME20}) [34] for the reference nuclides is shown. Panels (**a**) and (**b**) represent the results using T and T_Q, respectively. The calculated χ_n values are noted on the plots

Table 1 ME values and counts for the nuclides using T and T_Q are provided

	CSRe2011		Using T		Using T_Q		CSRe2023		Final
Atom	*ME* (keV)	Counts	*ME* (keV)	Counts	*ME* (keV)	Counts	*ME* (keV)	Counts	*ME* (keV)
^{63}Ge	−46921(37)	212	−46887(26)	391	−46927(18)	125	−46978(15)	279	−46957(25)
^{65}As	−46937(85)	37	−46798(61)	56	−46803(53)	15	−46806(42)	33	−46805(33)
^{67}Se	−46580(67)	67	−46482(43)	138	−46534(32)	46	−46549(20)	174	−46545(17)
^{71}Kr	−46320(141)	17	−46150(92)	30	−46038(72)	11	−46056(24)	148	−46054(23)

Results from prior IMS work based on the same experiment (CSRe2011) [23, 24] and a recent $B\rho$-IMS experiment (CSRe2023) [25, 26] are also included. The last column presents the weighted average ME values derived from T_Q and CSRe2023

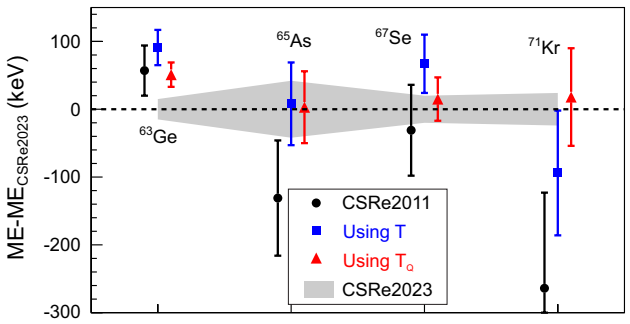

Fig. 8 For ^{63}Ge, ^{65}As, ^{67}Se, and ^{71}Kr, the ME differences between the values obtained from CSRe2011, using T and T_Q, respectively, and those from CSRe2023 are shown. The gray shadow indicates the mass uncertainty of CSRe2023

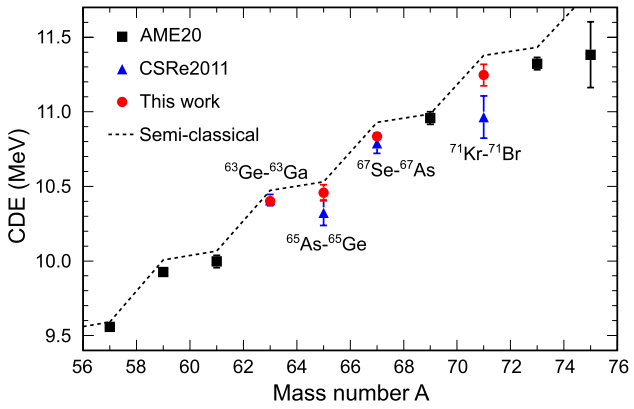

Fig. 9 Comparison of CDEs for $T_z = \pm 1/2$ mirror pairs, obtained using experimental masses from AME20 [41], CSRe2011 [23] and this work (using T_Q). The dotted line denotes the result from a semi-classical approach (see text)

as large as 2.2σ. Therefore, as shown in the last column of Table 1, the final ME value for ^{63}Ge was adjusted, and the weighted average uncertainty was increased to 25 keV, based on a birth ratio [36] of 2.17.

4 Discussion

The newly obtained *ME* values facilitate the calculation of CDE [37], which is the binding-energy difference between mirror nuclei. The CDE arises from differing Coulomb interactions in mirror nuclei due to their varying proton numbers and provides valuable insight into nuclear forces and symmetries [38].

For mirror pairs with $T_z = \pm 1/2$, the CDE can be extracted using the following equation:

$$CDE = ME_{>} - ME_{<} + \Delta_{\mathrm{nH}}, \tag{9}$$

where $ME_{>}$ and $ME_{<}$ represent the *ME* values of the proton-rich nucleus and its mirror partner, respectively, and Δ_{nH} =782.3470 keV represents the mass difference between the neutron and ^{1}H.

Given that the CDE can be expressed as the CED between mirror nuclei [39, 40], a semi-classical approach to the Coulomb energy [39] can be used to estimate the CDE.

$$E_{\mathrm{c}} = \left\{0.60Z^2 - 0.46Z^{4/3} - 0.15\left[1-(-1)^Z\right]\right\}\frac{e^2}{r_0 A^{1/3}}, \tag{10}$$

here, $r_0 = 1.2$ fm and $e^2 = 1.44$ MeV fm.

In Fig. 9, the CDEs obtained using experimental ME data from AME'20 [41], CSRe2011 [23] and the present study (using T_Q) are represented by different symbols. The CDEs calculated based on the semi-classical approach are depicted as dashed lines. The CDEs from this work align more closely with the semi-classical approach compared to those from CSRe2011 and indicate a more regular change behavior.

To clearly illustrate the variation in CDEs, the quantity

$$\Delta CDE(A) = CDE(A) - CDE(A-2) \tag{11}$$

was introduced to measure the difference in CDE between nuclei with mass number A and $A-2$.

In Fig. 10, experimental ΔCDEs are displayed alongside typical theoretical results. The zig-zag pattern in the theoretical ΔCDE is evident. Experimental ΔCDEs align well with

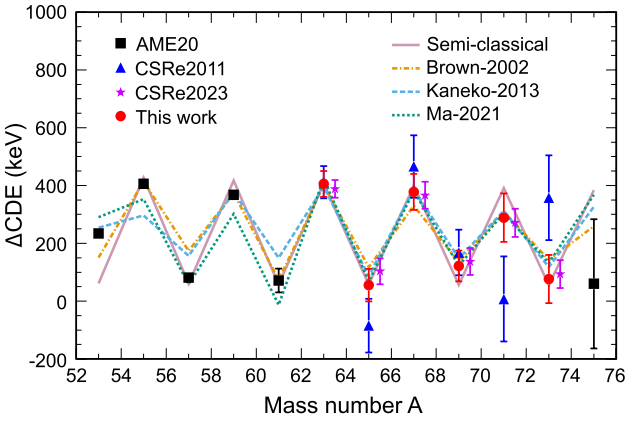

Fig. 10 Comparison of ΔCDEs. Experimental CDEs are indicted by symbols, while theoretical CDEs are presented as lines. For clarity, the CSRe2023 results (purple stars) are slightly right-shifted. Theoretical values are also presented, including those deduced from the semi-classical approach [39], and studies by Brown [42], Kaneko [38], and Ma [43]

various theoretical values for $A \geq 63$, except for those from CSRe2011. Deviations at $A = 71$ and $A = 73$ in CSRe2011 suggest abnormal staggering in ΔCDE, which was previously noted in Ref. [44] and attributed to a possible incorrect mass assignment for ^{69}Br due to its 574 keV isomer. However, using the updated mass value of ^{71}Kr obtained from this work (also CSRe2023), these deviations at $A = 71$ and $A = 73$ are removed, and the normal staggering pattern is restored.

While the ME values of ^{63}Ge from this work and CSRe2023 do not align well, the ΔCDEs at $A = 63$ (and 65) are consistent with each other and agree with theoretical calculations (Fig. 10). Therefore, future mass measurements of ^{63}Ge are required to resolve the mass discrepancy.

5 Conclusion and outlook

This study introduces Tune-IMS, a novel technique designed to enhance the performance of IMS. By effectively utilizing measured Q values, Tune-IMS was successfully implemented in IMS experiment at HIRFL-CSR. This approach led to a narrower revolution time spread, particularly for nuclides not satisfying the isochronous condition. Consequently, more precise mass values for fp shell nuclei ^{63}Ge, ^{65}As, ^{67}Se, and ^{71}Kr were re-determined, with validation supported by recent $B\rho$-IMS experiments. These redefined masses facilitated the calculation of CDEs, clarifying anomalies observed with previous mass values.

In Tune-IMS, the ion statistics are reduced due to the selection of Q values. To improve efficiency, a new type of TOF detector with positional sensitivity is currently under development [45]. This detector will provide additional position information, improving Q measurement performance and data utilization efficiency. Overall, Tune-IMS serves as a valuable complement to newly developed $B\rho$—defined IMS techniques and is particularly beneficial for conventional IMS systems equipped with a single TOF detector.

Author's contribution All authors contributed to the study conception and design. Material preparation, data collection and analysis were performed by Han-Yu Deng. The first draft of the manuscript was written by Han-Yu Deng and all authors commented on previous versions of the manuscript. All authors read and approved the final manuscript.

Data availability The data that support the findings of this study are openly available in Science Data Bank at https://cstr.cn/31253.11.sciencedb.j00186.00339 and https://www.doi.org/10.57760/sciencedb.j00186.00339.

Declarations

Conflict of interest The authors declare that they have no conflict of interest.

References

1. K. Blaum, High-accuracy mass spectrometry with stored ions. Phys. Rep. **425**, 1–78 (2006). https://doi.org/10.1016/j.physrep.2005.10.011
2. J. Clark, G. Savard, M. Mumpower et al., Precise mass measurements of radioactive nuclides for astrophysics. Eur. Phys. J. A **59**, 204 (2023). https://doi.org/10.1140/epja/s10050-023-01037-0
3. T. Yamaguchi, H. Koura, Y.A. Litvinov et al., Masses of exotic nuclei. Prog. Part. Nucl. Phys. **120**, 103882 (2021). https://doi.org/10.1016/j.ppnp.2021.103882
4. M.Z. Sun, X.H. Zhou, M. Wang et al., Precision mass measurements of short-lived nuclides at HIRFL-CSR in lanzhou. Front. Phys. **13**, 132112 (2018). https://doi.org/10.1007/s11467-018-0844-5
5. M. Hausmann, F. Attallah, K. Beckert et al., First isochronous mass spectrometry at the experimental storage ring ESR. Nucl. Instrum. Methods Phys. Res., Sect. A **446**, 569–580 (2000). https://doi.org/10.1016/S0168-9002(99)01192-4
6. M. Wang, H.S. Xu, J.W. Xia et al., First isochronous mass measurements at CSRe. Int. J. Mod. Phys. E **18**, 352–358 (2009). https://doi.org/10.1142/S0218301309012380
7. B. Sun, R. Knöbel, Y.A. Litvinov et al., Nuclear structure studies of short-lived neutron-rich nuclei with the novel large-scale isochronous mass spectrometry at the FRS-ESR facility. Nucl. Phys. A **812**, 1–12 (2008). https://doi.org/10.1016/j.nuclphysa.2008.08.013
8. Y.H. Zhang, H.S. Xu, Y.A. Litvinov et al., Mass measurements of the neutron-deficient ^{41}Ti, ^{45}Cr, ^{49}Fe, and ^{53}Ni nuclides: first test of the isobaric multiplet mass equation in *fp*-shell nuclei. Phys. Rev. Lett. **109**, 102501 (2012). https://doi.org/10.1103/PhysRevLett.109.102501
9. R. Knöbel, M. Diwisch, H. Geissel et al., New results from isochronous mass measurements of neutron-rich uranium fission fragments with the FRS-ESR-facility at GSI. Eur. Phys. J. A **52**, 138 (2016). https://doi.org/10.1140/epja/i2016-16138-6
10. X. Zhou, M. Wang, Y.H. Zhang et al., Charge resolution in the isochronous mass spectrometry and the mass of ^{51}Co. Nucl. Sci. Tech. **32**, 37 (2021). https://doi.org/10.1007/s41365-021-00876-0

11. Y.M. Xing, C.X. Yuan, M. Wang et al., Isochronous mass measurements of neutron-deficient nuclei from ^{112}Sn projectile fragmentation. Phys. Rev. C **107**, 014304 (2023). https://doi.org/10.1103/PhysRevC.107.014304
12. M.Z. Sun, Y. Yu, X.P. Wang et al., Ground-state mass of ^{22}Al and test of state-of-the-art ab initio calculations. Chin. Phys. C **48**, 034002 (2024). https://doi.org/10.1088/1674-1137/ad1a0a
13. M. Zhang, X. Zhou, M. Wang et al., $B\rho$-defined isochronous mass spectrometry and mass measurements of ^{58}Ni fragments. Eur. Phys. J. A **59**, 27 (2023). https://doi.org/10.1140/epja/s10050-023-00928-6
14. H. Geissel, R. Knöbel, Y.A. Litvinov et al., A new experimental approach for isochronous mass measurements of short-lived exotic nuclei with the FRS-ESR facility. Hyperfine Interact. **173**, 49–54 (2006). https://doi.org/10.1007/s10751-007-9541-4
15. J.H. Liu, X. Xu, P. Zhang et al., Improving the resolving power of isochronous mass spectrometry by employing an in-ring mechanical slit. Nucl. Instrum. Methods Phys. Res., Sect. B **463**, 138–142 (2020). https://doi.org/10.1016/j.nimb.2019.06.007
16. M. Wang, M. Zhang, X. Zhou et al., Bρ-defined isochronous mass spectrometry: An approach for high-precision mass measurements of short-lived nuclei. Phys. Rev. C **106**, L051301 (2022). https://doi.org/10.1103/PhysRevC.106.L051301
17. X. Zhou, M. Zhang, M. Wang et al., In-ring velocity measurement for isochronous mass spectrometry. Phys. Rev. Accel. Beams **24**, 042802 (2021). https://doi.org/10.1103/PhysRevAccelBeams.24.042802
18. X.L. Yan, R.J. Chen, M. Wang et al., Characterization of a double time-of-flight detector system for accurate velocity measurement in a storage ring using laser beams. Nucl. Instrum. Methods Phys. Res., Sect. A **931**, 52–59 (2019). https://doi.org/10.1016/j.nima.2019.03.058
19. Y.M. Xing, M. Wang, Y.H. Zhang et al., First isochronous mass measurements with two time-of-flight detectors at CSRe. Phys. Scr. **166**, 014010 (2015). https://doi.org/10.1088/0031-8949/2015/T166/014010
20. E. Courant, H. Snyder, Theory of the alternating-gradient synchrotron. Ann. Phys. **281**, 360–408 (2000). https://doi.org/10.1006/aphy.2000.6012
21. S.Y. Lee, Accelerator Physics, 4th Edition, (World Scientific, 2019). https://doi.org/10.1142/11111
22. T. Liao, C. Guo, X.L. Yan et al., Incoherent tune measurement of an ion storage ring using single ions. Phys. Rev. Accel. Beams **27**, 062801 (2024). https://doi.org/10.1103/PhysRevAccelBeams.27.062801
23. X.L. Tu, H.S. Xu, M. Wang et al., Direct mass measurements of short-lived A=2Z-1 nuclides ^{63}Ge, ^{65}As, ^{67}Se, and ^{71}Kr and their impact on nucleosynthesis in the *rp* process. Phys. Rev. Lett. **106**, 112501 (2011). https://doi.org/10.1103/PhysRevLett.106.112501
24. X.L. Tu, M. Wang, Y.A. Litvinov et al., Precision isochronous mass measurements at the storage ring CSRe in Lanzhou. Nucl. Instrum. Methods Phys. Res., Sect. A **654**, 213–218 (2011). https://doi.org/10.1016/j.nima.2011.07.018
25. X. Zhou, M. Wang, Y.H. Zhang et al., Mass measurements show slowdown of rapid proton capture process at waiting-point nucleus ^{64}Ge. Nat. Phys. **19**, 1091–1097 (2023). https://doi.org/10.1038/s41567-023-02034-2
26. M. Wang, Y.H. Zhang, X. Zhou et al., Mass measurement of upper *fp*-shell $N = Z - 2$ and $N = Z - 1$ nuclei and the importance of three-nucleon force along the $N = Z$ line. Phys. Rev. Lett. **130**, 192501 (2023). https://doi.org/10.1103/PhysRevLett.130.192501
27. Y.H. Zhang, Y.A. Litvinov, T. Uesaka et al., Storage ring mass spectrometry for nuclear structure and astrophysics research. Phys. Scr. **91**, 073002 (2016). https://doi.org/10.1088/0031-8949/91/7/073002
28. K. Wille, The Physics of Particle Accelerators: An Introduction, (Oxford University Press, 2001). https://doi.org/10.1093/oso/9780198505501.001.0001
29. B. Mei, X.L. Tu, M. Wang et al., A high performance time-of-flight detector applied to isochronous mass measurement at CSRe. Nucl. Instrum. Methods Phys. Res., Sect. A **624**, 109–113 (2010). https://doi.org/10.1016/j.nima.2010.09.001
30. Y.M. Xing, Y.H. Zhang, M. Wang et al., Particle identification and revolution time corrections for the isochronous mass spectrometry in storage rings. Nucl. Instrum. Methods Phys. Res., Sect. A **941**, 162331 (2019). https://doi.org/10.1016/j.nima.2019.06.072
31. J.D. Scargle, Studies in astronomical time series analysis. ii. statistical aspects of spectral analysis of unevenly spaced data. Astrophys. J. **263**, 835–853 (1982). https://doi.org/10.1086/160554
32. H. Nyquist, Certain topics in telegraph transmission theory. Trans. Am. Inst. Electr. Eng. **47**, 617–644 (1928). https://doi.org/10.1109/T-AIEE.1928.5055024
33. K. Pearson, VII. note on regression and inheritance in the case of two parents. Proc. R. Soc. Lond. **58**, 240 (1895). https://doi.org/10.1098/rspl.1895.0041
34. W.J. Huang, M. Wang, F.G. Kondev et al., The AME 2020 atomic mass evaluation (I). evaluation of input data, and adjustment procedures. Chin. Phys. C **45**, 030002 (2021). https://doi.org/10.1088/1674-1137/abddb0
35. Y.H. Zhang, P. Zhang, X.H. Zhou et al., Isochronous mass measurements of $T_z = -1$ *fp*-shell nuclei from projectile fragmentation of ^{58}Ni. Phys. Rev. C **98**, 014319 (2018). https://doi.org/10.1103/PhysRevC.98.014319
36. R.T. Birge, The calculation of errors by the method of least squares. Phys. Rev. **40**, 207–227 (1932). https://doi.org/10.1103/PhysRev.40.207
37. M. Bentley, S. Lenzi, Coulomb energy differences between high-spin states in isobaric multiplets. Prog. Part. Nucl. Phys. **59**, 497–561 (2007). https://doi.org/10.1016/j.ppnp.2006.10.001
38. K. Kaneko, Y. Sun, T. Mizusaki et al., Variation in displacement energies due to isospin-nonconserving rorces. Phys. Rev. Lett. **110**, 172505 (2013). https://doi.org/10.1103/PhysRevLett.110.172505
39. J.A. Nolen, J.P. Schiffer, Coulomb energies. Annu. Rev. Nucl. Part. Sci. **19**, 471–526 (1969). https://doi.org/10.1146/annurev.ns.19.120169.002351
40. S. Shlomo, Nuclear coulomb energies. Rep. Prog. Phys. **41**, 957–1026 (1978). https://doi.org/10.1088/0034-4885/41/7/001
41. M. Wang, W.J. Huang, F.G. Kondev et al., The AME 2020 atomic mass evaluation (II). Tables, graphs and references. Chin. Phys. C **45**, 030003 (2021). https://doi.org/10.1088/1674-1137/abddaf
42. B.A. Brown, R.R.C. Clement, H. Schatz et al., Proton drip-line calculations and the rp process. Phys. Rev. C **65**, 045802 (2002). https://doi.org/10.1103/PhysRevC.65.045802
43. C. Ma, Y.Y. Zong, S.Q. Zhang et al., Mass relations of mirror nuclei in terms of Coulomb energies based on relativistic continuum Hartree-Bogoliubov calculations. Phys. Rev. C **103**, 054326 (2021). https://doi.org/10.1103/PhysRevC.103.054326
44. X.L. Tu, Y. Sun, Y.H. Zhang et al., A survey of Coulomb displacement energies and questions on the anomalous behavior in the upper fp-shell. J. Phys. G Nucl. Part. Phys. **41**, 025104 (2014). https://doi.org/10.1088/0954-3899/41/2/025104
45. J.H. Liu, Z. Ge, Q. Wang et al., Electrostatic-lenses position-sensitive TOF MCP detector for beam diagnostics and new scheme for mass measurements at HIAF. Nucl. Sci. Tech. **30**, 152 (2019). https://doi.org/10.1007/s41365-019-0676-1